

Effective slip over partially filled microcavities and its possible failure

Zhouyang Ge^{1,*}, Hanna Holmgren^{2,†}, Martin Kronbichler^{3,‡}, Luca Brandt^{1,§} and Gunilla Kreiss^{2,¶}

¹ *Linné FLOW Centre and SeRC (Swedish e-Science Research Centre),*

KTH Mechanics, SE-100 44 Stockholm, Sweden

² *Division of Scientific Computing, Department of Information Technology,
Uppsala University, Box 337, 751 05 Uppsala, Sweden and*

³ *Institute for Computational Mechanics, Technical University of Munich,
Boltzmannstr. 15, 85748 Garching b. München, Germany*

Abstract Microscale roughness on an otherwise smooth hydrophobic surface can significantly reduce the resistance to an external liquid flow. We study static drag reduction over a lubricant-infused surface by looking at an array of two-dimensional transverse grooves partially filled with a second immiscible fluid. Numerical simulations at separate length scales are used to probe the static drag reduction property and the dynamic wetting behavior. Nano-scale phase field simulations are used to extract the characteristic contact line velocities. Micron-scale two-phase simulations using the level set method are used to model the interface deformation and the flow in and above the cavities. We study the dependence of the effective slip by varying viscosity ratios, capillary numbers, the static contact angle and the filling rate of the cavity (meaning the amount of lubricant fluid). We observe an increase of the effective slip with the cavity filling and identify a potentially new failure mode.

I. INTRODUCTION

Advances in microfluidics and nanotechnology have boosted a rapid development of surface engineering in the last two decades. Among the different effects of micro- and nano-patterned surfaces, often inspired by observation in nature, one remarkable finding is that the introduction of micro- or nanoscale roughness on an otherwise smooth hydrophobic surface can significantly reduce the resistance to an external liquid flow. This slippery effect, due to entrapment of gas or vapor pockets under the surface asperities (superhydrophobic Cassie state), was first observed in the experiment of a water flow through a water-repellent pipe [1]. Subsequently, a number of studies have demonstrated various levels of drag reduction [2–5], but also in some cases drag enhancement [6, 7]. Despite the discrepancies in the literature, a common

technological challenge for the application of superhydrophobic materials is their fragility [8]. Under high pressures or certain external forces, such as turbulent fluctuation or phase change, the surface texture can be partially or fully impregnated by the outer fluid (Cassie-to-Wenzel transition), causing the system to lose the features it was designed for [9, 10].

Lubricant-infused surfaces are an alternative when aiming to drag reduction. These, on the other hand, are more robust against pressure-induced failure, while displaying the same useful properties as conventional gas-cushioned superhydrophobic surfaces [25]. Two recent experiments have demonstrated, using microfabricated oil-impregnated pillars and grooves, separately, up to 16% drag reduction in laminar flow [11] and up to 14% drag reduction in turbulent flow [12]. In the case of the turbulent flow, the authors also tested superhydrophobic surfaces and measured approximately 10% drag reduction [12]. The amount of skin friction, depending on the viscosity ratio between the external fluid and the lubricant, typically increases as the lubricant becomes more viscous. However, there is also a proof-of-concept study showing improved drag reduction at less viscosity ratios

* zhoge@mech.kth.se

† hanna.holmgren@it.uu.se

‡ kronbichler@lhm.mw.tum.de

§ luca@mech.kth.se

¶ gunilla.kreiss@it.uu.se

with a hybrid surface design [13].

Analytically, the slippage over a superhydrophobic or liquid-infused surface is often characterized by an effective slip length. Analogous to the definition of the Navier slip, the effective slip length is an *averaged* quantity equal to the distance below the surface at which the velocity field would extrapolate to zero (to be distinguished from the *intrinsic* slip of molecular nature [9]). Extensive studies have been devoted to obtaining analytical expressions of the effective slip for two-dimensional longitudinal or transverse grooves, see *e.g.* [14–18]. The effect of the cavity geometry on the slip length, considered as the primary effect, has been predicted for different configurations, though the solutions typically rest on assumptions of either perfect slip or small deformation of the liquid-liquid interface, or non-wettability of the substrate by one fluid.

Understanding the dependence of the slip length on the imposed shear and contact angles in more realistic conditions may require a numerical approach, able to solve the details of the flow reducing the underlying assumptions. Due to the small dimension at the surface patterns, fluid inertia is negligible so that Stokes’ equation holds for each fluid, and the problem can be solved numerically using methods such as the lattice Boltzmann method [19, 20] and the phase field method [21], or alternatively through molecular dynamics simulations [24]. Physically, most previous studies focus on complete wetting of the surface asperities, corroborating the theoretical predictions. Interestingly, it was also found that a tiny depression of the meniscus into the cavity can result in a non-negligible decrease in the slip length, especially in the transverse case [17, 19, 21]. A recessed interface under external flow is often accompanied by unsteady motions, sometimes the contact line can even depin from the edge of a cavity [21]. When such depinning occurs, depending on the problem geometry, the authors of [21] predicted order-of-magnitude increases of the effective slip using a phase field simulation. We note however that the result was ob-

tained assuming no loss of the gas phase and a periodic computational domain. In practical applications, the surface patterns are open-ended and the lubricating gas or liquid is subject to drainage and evaporation/absorption by the liquid [25–27].

Considering the complex physics near a moving contact line, we propose a more detailed treatment for the modeling of partially filled cavities including the dynamics of the contact lines. The small-scale dynamics of moving contact lines represents a significant numerical difficulty, as it is several orders of magnitude smaller than global flow features [49]. At a global scale the flow and interface shape is governed by gravity and/or capillary forces [31], while at the molecular length scale the conventional hydrodynamic model break down and other models are necessary [31, 32]. Modeling contact line dynamics using standard two-phase models and the conventional no-slip boundary condition leads to a non-integrable stress singularity at the contact line [29, 33].

Various models have been proposed to model the dynamics of contact lines. One method is to replace the no-slip condition with a Navier slip condition [32, 34, 35] and prescribe the contact angle to the static angle, although the dynamic contact angle often differs from the static one [36, 37]. Another approach is to prescribe the contact angle according to an empirical law [38] or hydrodynamics theories [39–42]. In [34, 43–45] for example the Cox theory [39], based on the special case of lubrication, is used. A different approach is to use the phase field method where molecular processes are taken into account at the interface (including the contact line) by diffusion via the Cahn-Hilliard equation [30]. For more detailed reviews of different moving contact line models we refer to [28, 31, 35, 36].

Here, the multiscale model for dynamic contact lines presented in [50] is used. The idea is based on coupling a continuum-based two-phase flow model for the global flow to a local model for contact line dynamics. The local simulations are here on a scale of tens to hundreds of nano-meters, *i.e.* still at the con-

tinuum scale. These simulation are used to extract the characteristic contact line velocity, whereas micron-scale simulations model the interface deformation and the flow in and above the cavities. The phase field approach is used to obtain the contact line dynamics at the local scale, however other approaches can be used as well, e.g. molecular dynamics [47]. The coupling of the two models is here via the apparent contact angle and the local contact line velocity.

In the present work, we study the flow over microrough walls impregnated with a second lubricant fluid. We use the numerical simulations to probe the static drag reduction property and the dynamic wetting behavior. A potentially new failure mode is identified for partially filled transverse grooves under large external shear. Understanding of this drainage failure is instructive for improved robustness in surface design.

II. MICROCAVITIES PARTIALLY FILLED WITH LUBRICANTS

We consider the transverse flow over an array of regularly spaced square cavities illustrated in Fig. 1. The working fluid of viscosity μ_1 is driven by a constant shear $\dot{\gamma}$ in the x direction, imposed at a distance H above the floor. The cavities of length $L/2$ and depth $H/2$ are partially filled with a lubricant fluid of viscosity μ_2 . When the number of the microcavities is large, the system is equivalent to a single cavity with periodic boundary conditions. The solution at the steady state is determined from the incompressible Stokes equations, written in the non-dimensional form

$$\nabla \cdot \mathbf{u} = 0, \quad -\nabla p + \nabla \cdot [\mu_i (\nabla \mathbf{u} + \nabla \mathbf{u}^T)] = 0, \quad (1)$$

where $\mathbf{u} = (u, v)$ is the velocity, $p = p(x, y)$ the pressure, and $\mu_i = \tilde{\mu}_i / \tilde{\mu}_1$ ($i = 1$ or 2) the dimensionless viscosity (dimensional values are denoted with a tilde henceforth). For viscous flows, the velocity and its tangential derivatives are continuous along the interface [48]. The normal stress is discontinuous due to the surface tension $\tilde{\sigma}$ and the viscosity difference, giving the pressure jump (denoted as

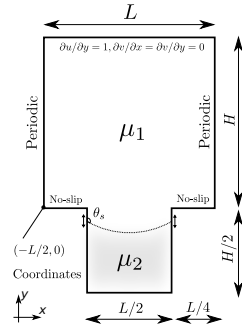


FIG. 1: Cross-section of a unit cavity and setup for the two-dimensional computational domain. The cavity of length $L/2$ and depth $H/2$ is partially filled with a lubricant fluid of viscosity μ_2 . The working fluid above with viscosity μ_1 is driven by a constant shear, $\partial u / \partial y = 1$. We also require zero normal stress on the top boundary to represent the far flow from the patterned surface. At steady state, this laminar flow is fully developed and periodic in the streamwise direction.

$$[A]_{\Gamma} = A_2 - A_1)$$

$$[p]_{\Gamma} = \frac{\kappa}{Ca} + 2[\mu]_{\Gamma} \mathbf{n}^T \cdot \nabla \mathbf{u} \cdot \mathbf{n}, \quad (2)$$

where \mathbf{n} is the outward-pointing normal at the interface Γ , κ its curvature, and $Ca = \tilde{\mu}_1 \dot{\gamma} \tilde{H} / \tilde{\sigma}$ the capillary number.

As we neglect the effect of inertia, Eqs. (1–2) are determined, fixing the geometry, by the following governing non-dimensional parameters: the viscosity ratio $\tilde{\mu}_2 / \tilde{\mu}_1$, the static contact angle θ_s and contact line velocity (function of the liquid and solid surface energies), the capillary number based on the imposed shear Ca , and the filling rate of the cavity $\delta^{-1} = H / (2|y|)$ (where $|y|$ is the distance from the top of the cavity to the initial contact point positions). Note that the filling rate defined here does not take the curvature of the interface into account, why it only makes sense to compare initial filling rates for cases where the initial interface shapes are the same. The

effect of the presence of the cavity and the corresponding apparent slip can be readily quantified by an effective slip length λ_e , defined as

$$\lambda_e = \frac{\bar{u}(H)}{\dot{\gamma}H} - 1, \quad (3)$$

where

$$\bar{u}(y) = \dot{\gamma}(y + \lambda_e H), \quad (4)$$

is the average velocity above the floor, assuming a linear flow profile with an additional slip $\lambda_e H$.

As we neither assume nor impose the shape of the lubricant surface in the cavity, but rather allow it to relax to its equilibrium under the external shear, one can introduce a second capillary number based on the contact line velocity, $Ca_c = \tilde{\mu}_2 \tilde{U}_c / \tilde{\sigma}$, where \tilde{U}_c is the characteristic contact line velocity (discussed later in Sec. III). The ratio between this velocity and the shear, $\chi = \tilde{U}_c / \dot{\gamma} \tilde{H}$, defines the relative variations of local slip with the imposed shear.

III. CONTACT LINE MODEL

This section presents the main ideas of the models in [50] and [49], and we refer to the respective references for further details. The main assumption is that there is a temporal and spatial scale separation between the local dynamics at the contact line and the global flow. This implies the local dynamics is in equilibrium for each apparent contact angle and no additional information from the global model is required, *i.e.* the contact line velocity U_c is only a function of the apparent contact angle θ_a [49]. The multiscale model consists of coupling a continuum-based two-phase flow model to a local model where the coupling is done via the apparent contact angle and the local contact line velocity.

The contact line velocity U_c is obtained from a local model in the are close to the contact line. Just as in [50] we use the model developed by Kronbichler and Kreiss in [49] for the local contact line dynamics. The model is

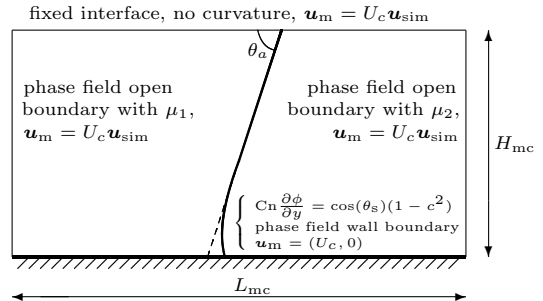


FIG. 2: Setup of the local phase field simulation domain according to [49].

based on solving an equilibrium scenario with the Cahn–Hilliard/Stokes system. The equilibrium is sought between the forces originating from the phase field model for an interface at the outer angle θ_a touching a wall of static contact angle θ_s [30] on the one hand and the motion U_c of the contact line on the other hand. In other words, the local simulations seeks an equilibrium of the viscous forces by the Stokes equations with the contact line diffusion in the Cahn–Hilliard equation.

The local simulation is performed in a box of height H_{mc} and length L_{mc} according to Fig. 2. The length L_{mc} is chosen as $L_{mc} = H_{mc} \left(\frac{1}{\tan(\theta_a)} + 0.5 \right)$ to fit an initially straight interface of angle θ_a within the domain plus some additional space to allow the flow to develop. In this box, the contact point velocity U_c is applied in terms of a moving frame of reference where the interface is kept fixed at the outer boundary but may move at the wall. For the correct contact point velocity U_c , the interface at the wall reaches a fixed position in the moving frame of reference, *i.e.* , it moves with constant speed relative to the wall, exactly balancing the force originating from the deviation in the contact angle with viscous dissipation in the flow field. The outer velocity boundary conditions are set according to the Huh–Scriven [29] similarity velocity u_{sim} scaled by the contact point velocity U_c .

Finding the contact point velocity U_c that hits the steady state is an inverse problem.

The algorithm starts with a tentative velocity $U_c^{(0)}$ as the speed of the contact line and records the deviation from the steady state after an initial transient as a function $f(U_c)$ [49]. The final velocity U_c is the limit of a sequence $U_c^{(0)}$ generated by a root finding algorithm to make $f(U_c)$ zero using a variant of inverse cubic interpolation.

The local contact line velocity U_c obtained from the phase field simulation is communicated to the global simulation via special boundary conditions at the global scale. The matching between the outer and inner solutions is done at an intermediate scale: close to the contact line at the outer scale but far from the contact line at the inner scale [49]. At this scale it is assumed the interface becomes asymptotically planar far from the contact line as seen from the inner scale [49], see Fig. 2. With this motivation the analytic Huh-Scriven similarity velocity [29] is used to formulate the global velocity boundary conditions. This analytic velocity depends on the local contact line velocity U_c obtained from the phase field model and in this way U_c is taken into account at the global level.

The Huh-Scriven velocity is not valid exactly at the contact line; there the phase field model describes the dynamics. Further, the analytic velocity has a singularity exactly at the contact line. With these motivations, parts of the intermediate matching region close to the contact line is excluded from the global simulation. The length scale of the excluded region should correspond to the length scale of the intermediate matching region. Along the new artificial boundary, the analytical velocity from the Huh-Scriven solution is applied as a velocity Dirichlet boundary condition for the global simulation. In this way the information about the contact point velocity U_c from the phase field model, *i.e.* the information about the movement of one single point, is transformed into a global velocity boundary condition along the whole modified boundary.

Remark: Our model implicitly assumes a perfectly smooth solid surface. In practice, a real surface may have random roughness or

defects which are smaller than the scale of the cavity, causing the interface to be pinned (*i.e.* contact angle hysteresis). There are several possibilities to take this effect into account in our model. One approach is to directly include the surface roughness in the local phase field domain by modifying the boundary (if the length scales of the roughness can be resolved by the local domain). Alternatively, contact angle hysteresis can be taken into account by extracting contact line velocities from molecular dynamics simulations where the surface chemistry and roughness is modeled at a nanoscale. A third option is to model hysteresis by modifying the relations in Fig. 3 to be $u_c = 0$ for a range of θ according to empirical values. However, to focus on the controlled physical effects, we assume our cavity has an ideal surface.

IV. NUMERICAL METHOD

A. The conservative level set method

The conservative level set method from [51] is used to keep track of the fluid-fluid interface and the moving contact line. The indicator function ϕ is a smoothed color function; the function smoothly switches value from +1 to -1 in a transition region around the interface. At the initial time, ϕ is computed from a signed distance function $d(\mathbf{x})$ around the interface by

$$\phi(\cdot, 0) = \tanh\left(\frac{d(\mathbf{x})}{\varepsilon}\right), \quad (5)$$

where ε is a parameter that controls the thickness of the transition region.

The level set function is advected in time by the underlying fluid velocity according to the Hamilton-Jacobi equation

$$\frac{\partial \phi}{\partial t} + \mathbf{u} \cdot \nabla \phi = 0. \quad (6)$$

After advecting the fluid interface, the surface tension force $\mathbf{F}_{st} = \sigma \kappa \mathbf{n} \delta_\Gamma$ is calculated, we refer to [52] for a detailed description.

Over time the level set function will lose its shape due to discretization errors and non-uniform velocity fields. To smooth the level set function and prevent the formation of very large gradients, ϕ has to be reinitialized with a regular interval. For the conservative level set method, this is done by solving the following equation to steady state

$$\frac{\partial \phi}{\partial \tau} + \nabla \cdot (\mathbf{n}(1 - \phi^2)) - \nabla \cdot (\mathbf{n} \varepsilon \nabla \phi \cdot \mathbf{n}) = 0, \quad (7)$$

where τ is a pseudo time step and \mathbf{n} is the interface normal. This equation calculates a smoothed color function by balancing diffusion in direction normal to the interface by a compressive flux. To fix the contact point position during the reinitialization we use a Dirichlet boundary condition at the boundaries with contact lines, see [50] for more details.

B. Artificial boundary

Just as in [50] the modified boundary (Sec. III) is parametrised using a so called bump function $f(x)$:

$$f(x) = \begin{cases} \delta \exp\left(1 - \left[1 - \left(\frac{x - x_{cp}}{w/2}\right)^2\right]^{-1}\right) & \text{if } |x - x_{cp}| < \frac{w}{2} \\ 0 & \text{otherwise,} \end{cases} \quad (8)$$

where δ and w is the height and width of the part of the domain that is excluded, and x_{cp} is the x -coordinate of the contact point position. Further, the simple approach to implement the global boundary conditions in [50] is also used here: the values of the velocity boundary function along the modified boundary are directly projected to the physical boundary.

C. Discretization and implementation

The governing equations are solved numerically using the two-phase flow solver described in [52], with suitable modifications to account for moving contact lines. The equations are discretized in space using the finite element

method and the solver is implemented in the C++ based finite element open source library deal.ii [53, 54]. For the level set function piecewise continuous linear shape functions on quadrilaterals, *i.e.* Q_1 elements, are used. For the Stokes equations we use the Taylor–Hood elements Q_2Q_1 , *i.e.* shape functions of degree two for each component of the velocity and of degree one for the pressure. With these elements the Babuška–Brezzi (inf-sup) condition [55] is fulfilled in order to guarantee the existence of a discrete solution.

For time stepping, each of the level set equation and Navier–Stokes equations are discretized using the second order accurate, implicit BDF-2 scheme. In order to avoid an expensive coupling between the Stokes part and the level set part (via the variables \mathbf{u} and ϕ) a temporal splitting scheme is introduced. In order to maintain second order accuracy in time, at each time step n an estimate of the level set function is extrapolated from the values at time steps $n - 1$ and $n - 2$. This estimate is used to evaluate an approximation of the surface tension force. With this surface tension force, the BDF-2 time step for the Stokes equations is then performed. Finally, the level set function is propagated in time, according to the velocity \mathbf{u}^n obtained from the Stokes step, again using the BDF-2 method. For more details about the discretizations see [52]. The resulting linear systems are solved by an iterative BiCGStab solver for the level set equation and by an iterative GMRES solver with block-triangular preconditioner according to [52].

V. RESULTS

We study the dependence of the effective slip over a microcavity partially filled with a second fluid by varying the viscosity ratio $\tilde{\mu}_2/\tilde{\mu}_1$, the capillary number $Ca = \tilde{\mu}_1 \dot{\gamma} \tilde{H}/\tilde{\sigma}$, the static contact angle θ_s , and the filling rate of the cavity $\delta^{-1} = H/(2|y|)$ (where $|y|$ is the distance from the top of the cavity to the initial contact point positions). The contact line velocity is obtained from the local phase field

model, using the physical properties of the two fluids as summarized in Tab. I. Here, only the working fluid viscosity is changing, as in the experiment [11], leading to a range of $\tilde{\mu}_2/\tilde{\mu}_1$ from 3.17 to 3.83×10^{-3} . Note that, in our model, the velocity ratio $\chi = \tilde{U}_c/(\dot{\gamma}\tilde{H})$ is also constant at a given shear as we do not vary the surface tension. This is done to reduce the number of parameters and focus on the single physical effects mentioned above. This implies that the Capillary number is varied by changing the applied shear. As an example, for a shear rate of $\dot{\gamma} = 800 \text{ s}^{-1}$ and a dimension of $\tilde{H} = 20 \text{ }\mu\text{m}$ (see estimates in [56]), the corresponding Ca increases from 1.92×10^{-3} to 1.59 for the different viscosities considered. We further modify Ca at a fixed χ to study the effect of interface deformation. Finally, the effect of θ_s on the effective slip is investigated artificially keeping the same contact line velocity.

TABLE I: Parameters for the working fluid (subscript 1) and lubricant fluid (subscript 2) in the present study.

$\tilde{\mu}_1 [\text{kg/ms}]$	$\tilde{\mu}_2 [\text{kg/ms}]$	$\tilde{\mu}_2/\tilde{\mu}_1$	$\tilde{\sigma} [\text{kg/s}^2]$	$\theta_s [\text{deg.}]$
0.0024	0.0076	3.17	0.02	80
0.1504	0.0076	0.0505	0.02	80
0.8942	0.0076	0.00850	0.02	80
1.9850	0.0076	0.00383	0.02	80

A. Local phase field results

The local phase field model described in Sec. III was used to precompute relations between contact angles and contact point velocities for the different viscosity ratios in Tab. I, for a static contact angle of $\theta_s = 80^\circ$. The non-dimensional height of the local box was $H_{\text{mc}} = 36$, the grid size $h = 36/128$ and time step $dt = 0.5$. Steady state was reached at a time of 2000, *i.e.* after 4000 time steps. The results are presented in Fig. 3. For the simulations in proceeding subsections we have also used static contact angles of $\theta_s = 105^\circ$. To

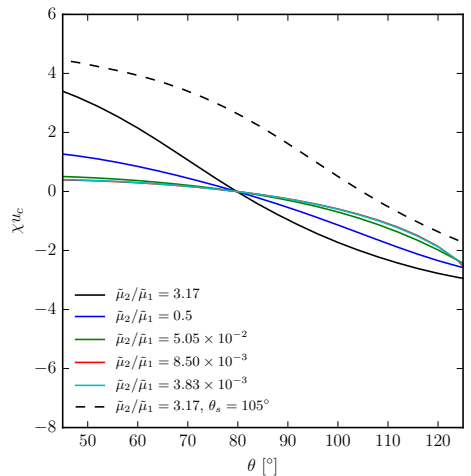


FIG. 3: (color online) Precomputed relations between contact angles and contact point velocities using the local phase field model.

obtain these relations (between contact angles and velocities) we have artificially shifted the corresponding curves to correspond to an angle of $\theta_s = 105^\circ$ instead, see the dashed line in Fig. 3 for an example.

The results for $\tilde{\mu}_2/\tilde{\mu}_1 = 3.17$ are significantly different from the other viscosity ratios. The main reason for the different behavior is the differences in the viscosities and the subsequent flow patterns. For the higher viscosity ratio, the working fluid is less viscous than the lubricant and the velocity gradients, supporting for the interface motion, are to a significant extent created in the working fluid. For the other viscosity ratios the working fluid is significantly more viscous and the velocity gradients, leading to shear forces, are mostly confined to the lubricant. This slows down the interface motion as a function of the angle, as seen in the region of contact angles between 40° and 110° . If the apparent contact angle deviates a lot from the static angle of 80° towards the lubricant, *i.e.* large apparent contact angles above 120° , the local model does not sufficiently represent the flow features of the large contrast any more, leading to large

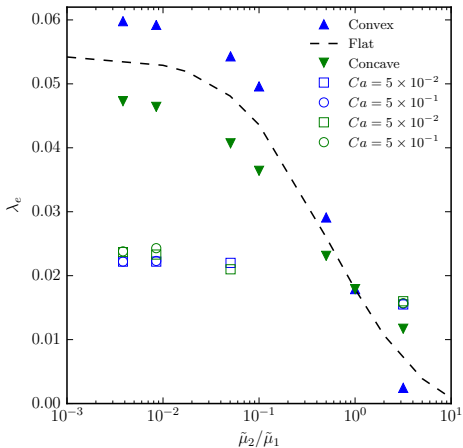


FIG. 4: (color online) Effective slip as function of viscosity ratio under various capillary numbers and filling rates. The dashed line represents a fixed flat interface filling the cavity. The filled symbols, upper blue and lower green triangles, stand for convex (80°) or concave (105°) interfaces pinned at the cavity corners in the zero capillary limit (*i.e.* fixed interface). The open symbols are the steady state solutions at filling rate $\delta^{-1} = 16.7$ for different Ca for convex (blue) and concave (green) interfaces.

unphysical values of the contact line velocity. In the numerical simulations presented here the computed contact angles never reach these large angles.

B. Static property: effective slip length

Numerical simulations for the set-up in Fig. 1 are performed using a grid with a spatial mesh size of $h = 0.00625$ and time steps in the range of $dt = 0.0001 - 0.0125$ (depending on the parameters). The height and width of the bump function (Sec. III) are $\delta = 2h$ and $w = 4h$ and the contact angle is calculated using fluid interface data at four grid cells inside the wall (see parameter D in [50]).

The effective slip length λ_e , defined in Eq.

(3), is plotted against the viscosity ratio under various capillary numbers and filling rates in Fig. 4. The results show steady state or fixed interface solutions. The dashed line is obtained by imposing a flat interface fully covering the cavity; this shows a continuous increase of the effective slip as the viscosity ratio reduces. The variation is nearly linear for $\tilde{\mu}_2/\tilde{\mu}_1 = 0.1 - 5$, while it begins to saturate for $\tilde{\mu}_2/\tilde{\mu}_1 < 0.1$. Analytical results showing similar trends in more general geometry can be found in [18]. The filled symbols in the figure indicate interfaces with the shape of a circular arc with a given contact angle (80° and 105°) in the zero capillary limit. When the interface is no longer flat, but still pinned at the two corners, λ_e differs appreciably depending on whether the lubricant protrudes outwards from the cavity (convex) or into the cavity (concave). Consistent with previous studies [7, 16], we found a larger slip length when the interface is convex (but below a critical angle over which high friction may occur [16]) for $\tilde{\mu}_2/\tilde{\mu}_1 < 1$. In our case, the slip of a convex shape can be over 30% larger than of a concave one. We also note that the trend becomes opposite when the lubricant is more viscous, a result that does not seem to have been reported before. The qualitative argument for such an asymmetry is rather straightforward. Similar to the reasoning in [15], the nonzero shear stress modified by a more viscous fluid will reduce the slip, hence a smaller slip length λ_e when the interface bows into the channel.

Finally, the non-filled symbols in the Fig. 4 report the results obtained with the contact-line model for different capillary numbers. The data pertain the steady state configuration, reached for shorter at higher Ca and verified to be independent of the size of the computational domain. Surprisingly, we find virtually no influence of the viscosity ratio or capillary number on the effective slip length for $\tilde{\mu}_2/\tilde{\mu}_1 \lesssim 0.1$. This independence from the viscosity ratio is peculiar, as one would expect more slip if the viscous dissipation is relatively low. However, as demonstrated in a recent analytical model for flat interfaces [18], the shear stress is constant along a fluid-fluid

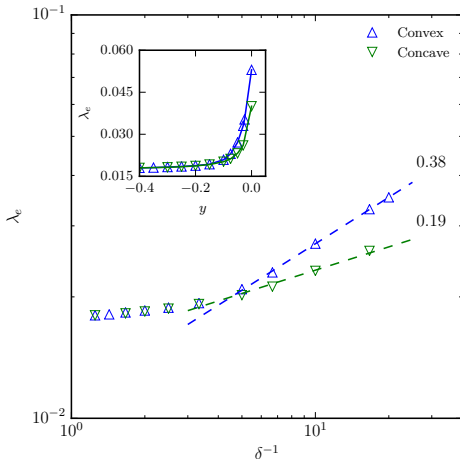


FIG. 5: Effective slip versus the filling rate of the cavity (defined with the height of the contact point) for a convex (80°) and a concave interface (105°) at $\tilde{\mu}_2/\tilde{\mu}_1 = 0.05$ in the zero capillary limit (minimum-energy interface). Dashed lines are the linear least squares fit for $\delta^{-1} > 5$, with slopes written beside. Inset: linear plot showing the sharp reduction of the slip length as the cavity becomes unfilled.

interface and the local slip length distribution depends only on the geometry of the patterned substrate. Considering that the interface protrudes only slightly, we can assume the argument above for flat interfaces to still apply and Eq. (2.19) in [18] indeed yields a nearly constant effective slip length for small $\tilde{\mu}_2/\tilde{\mu}_1$.

The results also indicate that the effective slip is rather insensitive to the capillary number. This can be explained by the fact that the deformation of the interface is rather small under the shear rate considered. Different experimental or numerical studies have reported conflicting effects of the shear (proportional to Ca), but typically the variation of the slip length is little below a critical Ca [20, 21]. Further increasing the capillary number and/or the shear can result in drainage of the lubricant from the cavity as will be discussed in more details later.

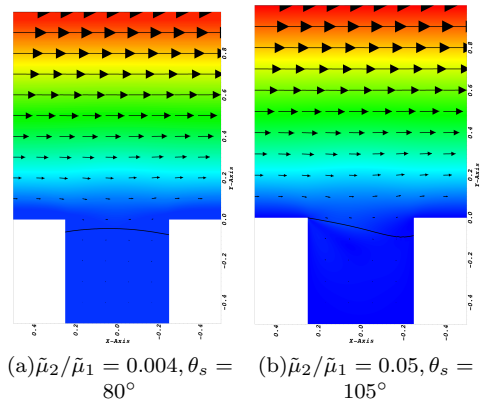


FIG. 6: (color online) Snapshots of typical shapes of the interface and of the instantaneous velocity field.

The above analysis implies that the filling rate may be the most important factor determining the effective slip length. We therefore consider in Fig. 5 the effective slip versus the filling rate of the cavity (defined with the height of the contact point) for a convex (80°) and a concave interface (105°) at $\tilde{\mu}_2/\tilde{\mu}_1 = 0.05$ in the zero capillary limit. Here, y is the vertical coordinate for the contact point position (see Fig. 1). Clearly, we see a strong dependence of λ_e on the depression of the liquid interface. The linear plot showing the rapid reduction of the slip length for both convex and concave surfaces is in good agreement with previous analytical and numerical studies [17, 19]. For the two interface curvatures considered, there seems to be a power law relation as illustrated in the log-log plot. Specifically, we find $\lambda_e \sim \delta^{-0.38}$ for the convex interface at static contact angle 80° , and $\lambda_e \sim \delta^{-0.19}$ for the concave interface at 105° . Our result confirms therefore the pronounced dependence of the interface depression, especially when it is small, for transverse grooves.

C. Dynamic behavior: lubricant drainage

The effective slip discussed above, induced by the imposed shear at the upper boundary

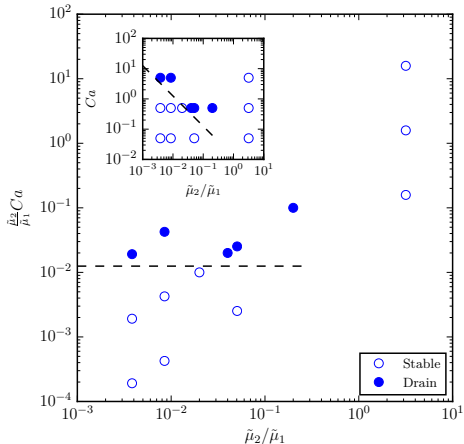


FIG. 7: Phase diagram in the cavity capillary-viscosity ratio plane ($\tilde{\mu}_2/\tilde{\mu}_1 Ca, \tilde{\mu}_2/\tilde{\mu}_1$) showing the boundary between stable meniscus and potential drainage of the microcavity. The inset reports the same data as function of the channel capillary number Ca .

of the computational domain, is a steady state result. Fig. 6 depicts two snapshots of the shear flow over a wetted cavity for two different viscosity ratios and static contact angles as the liquid interface tries to relax to its equilibrium position (starting from the solution in the zero capillary limit). The important difference between the behavior in Fig. 6(a) and (b) is that, in the first case the free surface remains stable beneath the cavity tip, while in the second case the upstream contact line has reached the corner. Since in both cases the contact lines are initially placed at a distance $y = -0.03$, the uprising motion in Fig. 6(b) implies a possible drainage of the lubricant from the cavity. We note that the depinning of a contact line from a sharp corner (*i.e.* drainage in our case) is a complex process, depending on the metastability of the wetting condition and the geometry of the corner [10]. Here, we simply stop the simulation when the contact line hits a corner, indicating the risk of a potential drainage (due to shear,

surface defeat, fluctuations, *etc.*).

To investigate the trigger for the cross-flow drainage, we run a series of simulations varying the capillary number and the viscosity ratio, at a fixed filling rate $\delta^{-1} = 16.7$ and a fixed contact angle of 80° . As illustrated in Fig. 7, increasing Ca for $\tilde{\mu}_2/\tilde{\mu}_1 < 1$ eventually leads to drainage. The result can be better interpreted using a cavity capillary number, based on the lubricant viscosity, $\tilde{\mu}_2/\tilde{\mu}_1 Ca$. Mapping the results on the $(\tilde{\mu}_2/\tilde{\mu}_1 Ca, \tilde{\mu}_2/\tilde{\mu}_1)$ plane indicates a critical capillary number above which the cavity can be fully wetted by the outer fluid. For the specific configuration investigated here, this critical capillary number $\tilde{\mu}_2/\tilde{\mu}_1 Ca = 0.0125$. It is worth noting that such a transition disappears for more viscous lubricants, as the contact line for the case $\tilde{\mu}_2/\tilde{\mu}_1 = 3.17$ stays inside the cavity, even when the lubricant capillary number is further increased by two orders of magnitude. Recalling that the effective slip is rather insensitive to the viscosity ratio at low filling rates, one can conclude that a more viscous lubricant might be preferable as more robust against shear-induced failures.

VI. CONCLUSIONS

In this paper, motivated by applications in nanoengineered patterned surfaces for robust drag reduction, we study the effective slip over an array of two-dimensional transverse grooves partially filled with a second immiscible fluid.

We use a hybrid multiscale approach to model the dynamics of the contact line between the two fluids at the cavity walls. In particular, we combine two separate simulation methods at different scales: we precompute the nanoscale contact line dynamics with a phase field method and use this as a modified boundary condition when solving the zero Reynolds number flow; we use the information from the contact line model in a finite element code to accurately evaluate the effective slip length of the microtextured surface. Our coupling assumes self-similarity of the velocity field in the vicinity of the moving con-

tact line. The approach is very general and it can be extended to include *e.g.* contact angle hysteresis according to the remark in Sec. III. Contact line friction can also be included by modifying the boundary condition in the phase field model [37].

We examine the effective slip in order to quantify the steady-state drag-reducing property of the surface with transverse cavities of micron size. Here, we fix the geometry and vary the cavity-to-outer viscosity ratio, capillary number, static contact angle, and cavity filling rate. Our results confirm the previously observed increase of the effective slip with the cavity filling, as the shear stress near a cavity strongly depends on the meniscus position in transverse cases. In addition, we find the influence of the viscosity ratio or capillary number to be rather weak, a result that appears counter-intuitive at first. This diminished effect is partly due to the moderate filling configuration, partly due to the relatively low shear applied.

Further increasing the capillary number, we observe a transition from stable lubricant infusion to lubricant depletion, identified here as the contact line reaches the cavity tip. For

lubricant impregnated surfaces, this can potentially lead to drainage induced by the extreme external shear. We show that there exists a critical capillary number, based on the lubricant viscosity, above which drainage can occur and which is almost constant for low viscosity ratios. However, differently from the shear-driven drainage observed in longitudinal grooves, this new cross-flow failure mode appears to be suppressed by a high lubricant viscosity. Our prediction therefore suggests that a less viscous lubricant may not necessarily be the most robust, also given that the performance is weakly sensitive to the viscosity ratio.

ACKNOWLEDGEMENTS

We thank Shervin Bagheri and Uģis Lācis for calling our attention on the problem of micropatterned surfaces. We also thank Mauro Chinappi for many helpful discussions. This project is funded by the European Union Horizon 2020 research and innovation programme under Grant Agreement No. 664823 and the Swedish Research Council.

-
- [1] K. Watanabe, Yanuar, and H. Udagawa, *J. Fluid Mech.* **381**, 225–238 (1999).
 - [2] J. Ou, B. Perot, and J. P. Rothstein, *Phys. Fluids* **16**, 4635 (2004).
 - [3] D. Schäffel, K. Koynov, D. Vollmer, H.-J. Butt, and C. Schönecker, *Phys. Rev. Lett.* **116**, 134501 (2016).
 - [4] C. Lee, C.-H. Choi, and C.-J. Kim, *Exp. Fluids* **57**, 176 (2016).
 - [5] C.-H. Choi, and C.-J. Kim, *Phys. Rev. Lett.* **96**, 066001 (2006).
 - [6] A. Steinberger, C. Cottin-Bizonne, P. Kleimann, and E. Charlaix, *Nat. Mater.* **6**, 665 (2007).
 - [7] E. Karatay, A.S. Haase, C.W. Visser, C. Sun, D. Lohse, P.A. Tsai, R.G.H. Lammertink, *Proc. Natl. Acad. Sci.* **110**, 8422–8426 (2013).
 - [8] L. Bocquet, and E. Lauga, *Nat. Mater.* **10**, 334 (2011).
 - [9] D. Gentili, G. Bolognesi, A. Giacomello, M. Chinappi, and C. M. Casciola, *Microfluid Nanofluid* **166**, 1009–1018 (2014).
 - [10] A. Giacomello, M. Chinappi, S. Meloni, and C. M. Casciola, *Phys. Rev. Fluids* **109**, 226102 (2012).
 - [11] B. R. Solomon, K. S. Khalil, and K. K. Varanasi, *Langmuir* **30**, 10970–10976 (2014).
 - [12] B. J. Rosenberg, T. V. Buren, M. K. Fu, and A. J. Smits, *Phys. Fluids* **28**, 015103 (2016).
 - [13] A. A. Hemeda, and H. Vahedi Tafreshi, *Langmuir* **32**, 2955–2962 (2016).
 - [14] E. Lauga, and H. A. Stone, *J. Fluid Mech.* **489**, 55–77 (2003).
 - [15] M. Sbragalia, and A. Prosperetti, *Phys. Fluids* **19**, 043603 (2007).
 - [16] A. M. J. Davis, and E. Lauga, *Phys. Fluids* **21**, 011701 (2009).

- [17] C.-O. Ng, and C. Y. Wang, *Phys. Fluids* **21**, 013602 (2009).
- [18] C. Schönecker, T. Baier, and S. Hardt, *J. Fluid Mech.* **740**, 168–195 (2014).
- [19] T. Biben, and L. Joly, *Phys. Rev. Lett.* **100**, 186103 (2008).
- [20] J. Hyvälä, and J. Harting, *Phys. Rev. Lett.* **100**, 246001 (2008).
- [21] P. Gao, and J. J. Feng, *Phys. Fluids* **21**, 102102 (2009).
- [22] C. J. Teo, and B. C. Microfluid Nanofluid **9**:499–511 (2010).
- [23] E. Alinovi, and A. Bottaro, *in press*.
- [24] N. V. Priezjev, A. A. Darhuber, and S. M. Troian, *Phys. Rev. E* **710**, 041608 (2005).
- [25] J. S. Wexler, I. Jacobi, and H. A. Stone, *Phys. Rev. Lett.* **114**, 168301 (2015).
- [26] I. Jacobi, J. S. Wexler, and H. A. Stone, *Phys. Fluids* **27**, 082101 (2015).
- [27] Y. Liu, J. S. Wexler, C. Schönecker, and H. A. Stone, *Phys. Rev. Fluids* **1**, 074003 (2016).
- [28] T. D. Blake, *J. Colloid Int. Sci.* **299**, No. 1-13 (2006).
- [29] C. Huh and L. E. Scriven, *J. Colloid Int. Sci.* **35**, No. 1 (1971).
- [30] D. Jacqmin, *J. Fluid Mech.* **402**, 57–88 (2000).
- [31] G. Lu, X.-D. Wang and Y.-Y. Adv. Colloid Interface Sci. **236**, 43–62 (2016).
- [32] J. H. Snoeijer and B. Andreotti. Annual review of fluid mechanics. **45**, 269 – 292 (2013).
- [33] E. B. Dussan V. and S. H. Davis. *J. Fluid Mech.* **65**, 71–95 (1974).
- [34] Y. Sui and P. D. Spelt. *J. Comput. Phys.* **242**, 37–52 (2013).
- [35] D. Legendre and M. Maglio. *Comput. Fluids.* **113**, 2–13 (2015).
- [36] Y. Sui, H. Ding and P. D. Spelt. Annual Review of Fluid Mechanics. **46**, 97–119 (2014).
- [37] M. D.-Q., J. Shiomi and G. Amberg. *EPL (Europhysics Letters)*. **110**, 46002 (2015).
- [38] D. Bonn, J. Eggers, J. Indekeu and J. Meunier and E. Rolley. *Rev. Mod. Phys.* **2**, 739–805 (2009).
- [39] R. G. Cox. *J. Fluid Mech.* **168**, 169–194 (1986).
- [40] R. G. Cox. *J. Fluid Mech.* **357**, 249–278 (1998).
- [41] L. M. Hocking and A. D. Rivers. *J. Fluid Mech.* **121**, 425–442 (1982).
- [42] C. G. Ngan and E. B. Dussan. Cambridge University Press. **209**, 191226 (1989).
- [43] J.-B. Dupont and D. Legendre. *J. Comput. Phys.* **229**, 2453–2478 (2010).
- [44] K. Yokoi, D. Vadiello, J. Hinch and I. Hutchings. *Phys. Fluids*. **21**, (2009).
- [45] S. Afkhami, S. Zaleski and M. Bussmann. *J. Comput. Phys.* **228**, 5370–5389 (2009).
- [46] W. Ren, and W. E, *Phys. Fluids* **19**, 022101 (2007).
- [47] P. Johansson, A. Carlson, and B. Hess, *J. Fluid Mech.* **781**, 695–711 (2015).
- [48] G. K. Batchelor, *An introduction to fluid dynamics*, (Cambridge university press, 2000).
- [49] M. Kronbichler and G. Kreiss, *J. Comp. Multiphase Flows* **0(0)** 1–13 (2017).
- [50] H. Holmgren and G. Kreiss. *A computational multiscale model for contact line dynamics*. ArXiv e-prints:1709.04917 (2017).
- [51] E. Olsson and G. Kreiss. *J. Comput. Phys.* **210**, 225 - 246 (2005).
- [52] M. Kronbichler, A. Diagne and H. Holmgren. *Int. J. High Perform. Comput. Appl.* , 1–22 (2016).
- [53] W. Bangerth, T. Heister, L. Heltai, G. Kanschat, M. Kronbichler, M. Maier and B. Turcksin. *Archive of Numerical Software*. **4**, 1–11 (2016).
- [54] W. Bangerth, R. Hartmann and G. Kanschat. *ACM Trans. Math. Softw.* **33**, (2007).
- [55] V. Girault and P.-A. Raviart. *J. Appl. Math. Mech.* , 579–579 (1986).
- [56] We estimate the dimensional shear rate at the upper boundary of our computational domain from the flow rate of the Hele-Shaw channel in [25] (2 mL/min through a cross-section of $180\text{ }\mu\text{m} \times 7\text{ mm}$). Assuming a parabolic velocity profile the reference velocity at $\dot{H} = 20\text{ }\mu\text{m}$ is $\bar{U} = 0.016\text{ m/s}$, leading to a shear rate of $\dot{\gamma} = 800\text{ s}^{-1}$.